Earth Planets Space, **65**, 1271–1283, 2013

Swarm SCARF Dedicated Ionospheric Field Inversion chain

Arnaud Chulliat, Pierre Vigneron, Erwan Thébault, Olivier Sirol, and Gauthier Hulot

Equipe de Géomagnétisme, Institut de Physique du Globe de Paris, Sorbonne Paris Cité, Université Paris Diderot, UMR 7154 CNRS, F-75005 Paris, France

(Received April 2, 2013; Revised August 25, 2013; Accepted August 26, 2013; Online published November 22, 2013)

The geomagnetic daily variation at mid-to-low latitudes, referred to as the geomagnetic Sq field, is generated by electrical currents within the conducting layers of the ionosphere on the dayside of the Earth. It is enhanced in a narrow equatorial band, due to the equatorial electrojet. The upcoming ESA *Swarm* satellite mission, to be launched end of 2013, will consist of three satellites in low-Earth orbit, providing a dense spatial and temporal coverage of the ionospheric Sq field. A Satellite Constellation Application and Research Facility (SCARF) has been set up by a consortium of research institutions, aiming at producing various level-2 data products during the *Swarm* mission. The Dedicated Ionospheric Field Inversion (DIFI) chain is a SCARF algorithm calculating global, spherical harmonic models of the Sq field at quiet times. It describes seasonal and solar cycle variations, separates primary and induced magnetic fields based upon advanced 3D-models of the mantle electrical conductivity, and relies on core, lithospheric and magnetospheric field models derived from other SCARF algorithms for removing non-ionospheric fields from the data. The DIFI chain was thoroughly tested on synthetic data during the SCARF preparation phase; it is now ready to be used for deriving models from real *Swarm* data.

Key words: *Swarm*, ionosphere, inversion, geomagnetism, space magnetometry.

1. Introduction

A small fraction of the Earth's magnetic field is generated by electrical currents within the conductive layers of the ionosphere, near 110 km altitude. On geomagnetically quiet days, at mid-to-low latitudes, the ionospheric magnetic field has an amplitude of 10 to 50 nT on the ground and is referred to as the "Sq" magnetic field (see, e.g., Richmond and Thayer, 2000). It undergoes a characteristic daily variation, visible in geomagnetic observatory recordings, where the Z component increases (in absolute value) from sunrise to noon and decreases from noon to sunset. In a $\pm 5^\circ$ latitudinal band centered on the geomagnetic dip-equator, the amplitude of this daily variation is even larger and can reach up to 100 nT on the ground around noon. The ionospheric field in this band is caused by the equatorial electrojet, a thin current flowing eastward along the geomagnetic dip-equator.

Global spherical harmonic models of the Sq field have classically been determined from observatory data, relying on the global observatory network. Such models (e.g., Schmucker, 1999a, b; Takeda, 2002) provide a description of the large-scale current system generating the Sq field, as well as its seasonal and solar cycle variability. Use of magnetic measurements from low-Earth orbiting satellites such as Ørsted and CHAMP makes it possible to model the Sq field up to higher spherical harmonic degrees, and to also model the equatorial electrojet field (Sabaka *et al*., 2002, 2004). However, satellite data are collected above the ionosphere. They cannot separate the primary ionospheric field from the secondary, induced field generated by electrical currents within Earth's mantle. Such a separation is possible, however, if a pre-determined mantle conductivity model is available.

The upcoming ESA *Swarm* satellite mission, to be launched in 2013, will provide measurements of the Earth's magnetic field with unprecedented precision from three identical satellites orbiting at different altitudes and local times (Friis-Christensen *et al*., 2006). Several research institutions have teamed up with ESA to form the *Swarm* Satellite Constellation Application and Research Facility (SCARF), a distributed processing facility that will produce geomagnetic field models during the *Swarm* mission (Olsen *et al*., 2013). Two of these models will be spherical harmonic descriptions of the ionospheric magnetic field at mid-to-low latitudes, i.e., below 55° dipole latitude. One of them will be calculated as part of a comprehensive inversion, where all major sources of the geomagnetic field will be calculated simultaneously (Sabaka *et al*., 2013); the other will be calculated through a dedicated inversion, after removing the magnetic fields generated by other sources from the data.

In the present paper, we introduce the *Swarm* Dedicated Ionospheric Field Inversion (DIFI) algorithm (Section 2), which will be used for calculating the dedicated ionospheric field from *Swarm* data. The DIFI chain takes into account the seasonal and solar cycle variability of the field. It was thoroughly tested during its development phase using synthetic data. Results of these tests are presented in Section 3. The DIFI chain is one of the three chains devel-

doi:10.5047/eps.2013.08.006

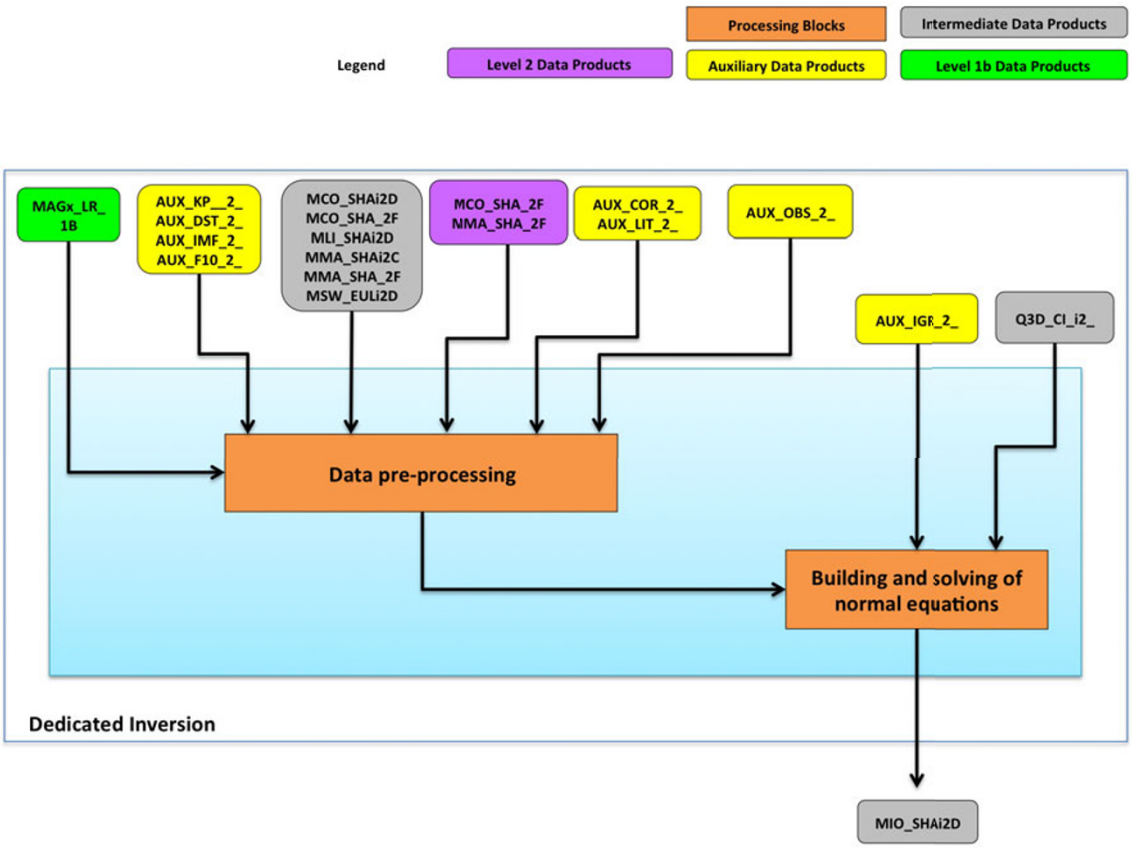

Fig. 1. Flowchart of the DIFI algorithm.

oped by IPGP within SCARF; other chains are the Dedicated Lithospheric Field Inversion (DLFI) chain (Thébault *et al.*, 2013) and the Equatorial Electric Field (EEF) inversion chain (with NOAA, Alken *et al.*, 2013).

2. DIFI Algorithm

2.1 Data pre-processing

During the exploitation phase, the DIFI algorithm will be used to calculate two types of models: ionospheric field models calculated over at least one year of data, which will include a description of the seasonal variation of model coefficients, and ionospheric field models calculated over less than one year of data (typically three to six months), with coefficients assumed constant with respect to season. The second type of model will be calculated only during the first year of the mission, to provide a first model within a few months after the commissioning phase. In what follows, we describe the algorithm to be used for the calculation of a full model, including seasonal variation, assuming one full year of level 1b magnetic data is available as input.

By default, the DIFI algorithm reads all level 1b vector magnetic data from *Swarm* A, one of the two satellites orbiting side-by-side at about 460 km altitude, and from *Swarm* C, the satellite orbiting at a higher altitude of about 530 km, in a different local time sector. Several failure cases have been investigated as part of the preparation phase within SCARF, for example the complete failure of one satellite or the lack of vector data from one of the satellites. If such an unhappy event were to occur, the DIFI algorithm would still be able to ingest reduced level 1b dataset. In what follows, we describe the nominal scenario where level 1b vector magnetic data are available from both *Swarm* A and C satellites.

The first block of the DIFI algorithm consists in reading all level 1b *Swarm* magnetic field data available during the considered time interval, selecting data at magnetically quiet times, and correcting these data for non-ionospheric fields. This block is refered to as "Data pre-processing" in Fig. 1. Level 1b magnetic data are selected using standard geomagnetic indices: K_{p}, D_{st} and the interplanetary magnetic field (IMF) B_y and B_z components. The minimum and maximum acceptable values for these parameters will be adjusted for each real dataset, in order to maximize spatial, local time and seasonal data coverage, while minimizing the overall magnitude of disturbance fields. Also, in order to minimize the size of the dataset to be inverted, level 1b data are decimated to one sample every 15 s prior to the inversion.

The next step of the pre-processing block is data correction. It aims at removing non-ionospheric contributions from the total vector field recorded by each satellite. Three main sources are considered: the core, the lithosphere and the electrical currents in the magnetosphere. By default, SCARF dedicated (Hamilton, 2013; Rother *et al.*, 2013; Thébault *et al.*, 2013) and/or comprehensive (Sabaka *et al.*, 2013) models are used to remove contributions from these sources. If needed, non-SCARF, auxiliary models will be considered during the exploitation phase to improve the

quality of the final model.

Observatory data (hourly mean values, see Macmillan and Olsen, 2013) can also be used by the DIFI algorithm, although not in the default mode. These data are preprocessed in a similar way: first, they are selected according to geomagnetic K_p and D_st indices, as well as IMF B_y and B_z components; second, they are corrected for the core, lithospheric and magnetospherie fields using the same dedicated or comprehensive SCARF models. Observatory biases, i.e., the small-scale lithospheric field not described by these models, are left as variables to be determined by the inversion.

2.2 Model parameterization

The DIFI algorithm relies on the same ionospheric field model parameterization as the comprehensive models (see, e.g., Sabaka *et al*., 2000, 2002, 2013). In what follows, we briefly summarize the main features of this parameterization, using similar matrix notations as Sabaka *et al*. (2000).

Primary sources of the ionospheric magnetic field at mid-to-low latitudes are electrical currents flowing in the E-region of the ionosphere, at about $h = 110$ km altitude. The time-varying magnetic field generated by these currents induces secondary currents in the upper layers of the Earth's electrically conducting mantle, which in turn contribute to the total ionospheric magnetic field. The spherical harmonic modeling of the ionospheric magnetic field relies on the assumption that *Swarm* satellites fly above these ionospheric sources. As a consequence, the ionospheric magnetic field $\boldsymbol{B}$ (i.e., observations minus contributions from the core, lithosphere and magnetosphere) may be expressed as $\boldsymbol{B} = -\boldsymbol{\nabla} V$, where V is a magnetic potential.

Let us introduce the following set of basis functions:

$$S^m_{nsp,e}(r,\theta_d,\phi_d,t,t_m) = a\left(\frac{r}{a}\right)^n P^m_n(\theta_d)\exp[i(m\phi_d+\omega_s st+\omega_p pt_m)] \quad (1)$$

$$S^m_{nsp,i}(r,\theta_d,\phi_d,t,t_m) = a\left(\frac{a}{r}\right)^{n+1} P^m_n(\theta_d)\exp[i(m\phi_d+\omega_s st+\omega_p pt_m)] \quad (2)$$

where r is the radius, θ_d the dipole colatitude, ϕ_d the dipole longitude, t (expressed in yrs) the season counted from January 1st, at 00:00 universal time, t_m (expressed in hrs) the magnetic universal time, a the mean Earth radius ($a = 6371.2$ km), P^m_n the Schmidt normalized associated Legendre function of degree n and order m, $\omega_s = 2\pi$ rad/yr the fundamental angular frequency for seasonal variation, $\omega_p = 2\pi/24$ rad/hr the fundamental angular frequency for diurnal variation, s and p the associated wavenumbers. The magnetic universal time is defined as

$$t_m = (180 - \phi_{d,s})/15 \quad (3)$$

where $\phi_{d,s}$ is the dipole longitude of the sub-solar point (defined as the point on the Earth's surface closest to the sun), expressed in degrees. Then the potential V may be uniquely expressed in the dipole reference frame as:

$$V = Re\{\,\boldsymbol{\epsilon}^H\boldsymbol{S_e} + \boldsymbol{\iota}^H\boldsymbol{S_i}\} \qquad \text{for } a < r < a+h \quad (4)$$

$$V = Re\{(\,\boldsymbol{\epsilon}'^H + \boldsymbol{\iota}^H)\boldsymbol{S_i}\} \qquad \text{for } r > a+h \quad (5)$$

where $\boldsymbol{\epsilon}$, $\boldsymbol{\iota}$ and $\boldsymbol{\epsilon}'$ are vectors of complex coefficients $(\epsilon^m_{nsp})^*$, $(\iota^m_{nsp})^*$ and $(\epsilon'^m_{nsp})^*$, respectively, and $\boldsymbol{S_e}$ and $\boldsymbol{S_i}$ are the vectors of the $S^m_{nsp,e}$ and $S^m_{nsp,i}$, respectively. Here $Re\{z\}$ denotes the real part of complex number z, z^* denotes its conjugate and $\boldsymbol{A}^H$ denotes the conjugate transpose of vector or matrix $\boldsymbol{A}$. At ground altitude, the $S^m_{nsp,e}$ basis functions and $\boldsymbol{\epsilon}$ coefficients describe the primary ionospheric field, while the $S^m_{nsp,i}$ basis functions and $\boldsymbol{\iota}$ coefficients describe the secondary (i.e., induced) ionospheric field. At satellite altitude, all sources are internal and therefore the $S^m_{nsp,i}$ basis functions describe the total field. The $\boldsymbol{\iota}$ coefficients are the same at ground and at satellite altitude.

The induced field is related to the primary field through a transfer function, which may be expressed in matrix form as

$$\boldsymbol{\iota} = \boldsymbol{Q}\,\boldsymbol{\epsilon}\,. \quad (6)$$

For a 1D mantle conductivity, the $\boldsymbol{Q}$ matrix is diagonal, while for a 3D conductivity it is dense for one single frequency, and block-diagonal for multiple frequencies. The DIFI algorithm can deal with both the 1D and 3D cases. Noting that the radial component of the ionospheric field is continuous through the current sheet at $r = a + h$, we necessarily have (by taking the radial derivative of $S^m_{nsp,e}$ and $S^m_{nsp,i}$ at $r = a + h$)

$$\boldsymbol{\epsilon}' = \boldsymbol{C}\,\boldsymbol{\epsilon} \quad (7)$$

where $\boldsymbol{C}$ is a diagonal real matrix with the following elements

$$c^m_{nsp} = -\left(\frac{n}{n+1}\right)\left(\frac{a+h}{a}\right)^{2n+1}. \quad (8)$$

Therefore, (4) and (5) become

$$V = Re\{\,\boldsymbol{\epsilon}^H(\boldsymbol{S_e} + \boldsymbol{Q}^H\boldsymbol{S_i})\} \qquad \text{for } a < r < a+h \quad (9)$$

$$V = Re\{\,\boldsymbol{\epsilon}^H(\boldsymbol{C} + \boldsymbol{Q}^H)\boldsymbol{S_i}\} \qquad \text{for } r > a+h \quad (10)$$

It is advantageous to model the ionospheric field in the quasi-dipole (QD) coordinate system (Richmond, 1995; Emmert *et al*., 2010), which follows the geometry of the Earth's main magnetic field. This is mostly because the equatorial electrojet flows along the geomagnetic dip-equator, which is bended with respect to the dipole equator in the South American sector. Using QD coordinates helps minimizing the total number of parameters to be determined. The DIFI algorithm relies on the same QD basis function as Sabaka *et al*. (2000),

$$T^l_{ksp,e}(r,\theta_q,\phi_q,t,t_m) = \sum_{n=1}^{N_\mathrm{max}}\sum_{m=-\min(n,M_\mathrm{max})}^{\min(n,M_\mathrm{max})}\left(d^{lm}_{kn}\right)^*\left(\frac{a}{a+h}\right)^{n-1} \times S^m_{nsp,e}(r,\theta_d,\phi_d,t,t_m) \quad (11)$$

$$T^l_{ksp,i}(r,\theta_q,\phi_q,t,t_m) = \sum_{n=1}^{N_\mathrm{max}}\sum_{m=-\min(n,M_\mathrm{max})}^{\min(n,M_\mathrm{max})}\left(d^{lm}_{kn}\right)^*\left(\frac{a+h}{a}\right)^{n+2} \times S^m_{nsp,i}(r,\theta_d,\phi_d,t,t_m) \quad (12)$$

where (θ_q, ϕ_q) are the QD colatitude and longitude, $h = 110$ km is the altitude of the ionospheric electrical currents,

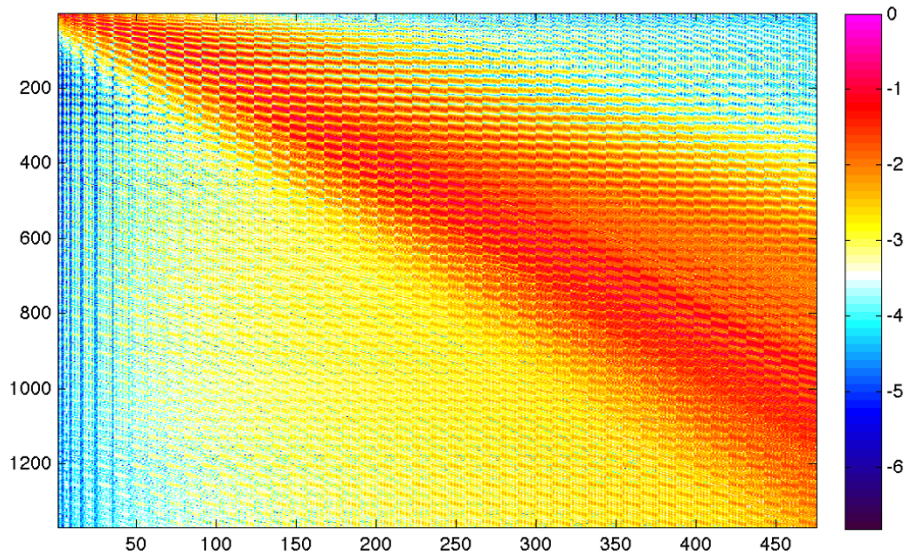

Fig. 2. Modulus of the complex elements of the $\boldsymbol{D}$ matrix relating dipole and quasi-dipole spherical harmonics through Eq. (13), for $K_{\max} = 45$, $L_{\max} = 5$, $N_{\max} = 60$, $M_{\max} = 12$. The color scale is in powers of 10. There are $N_q = 475$ quasi-dipole harmonics (abscissae) and $N_d = 1368$ dipole harmonics (ordinates).

Table 1. General structure of a MIO_SHA product file. All notations are defined in the main text (Subsections 2.2 and 2.4), except θ_{NGP} and ϕ_{NGP} which stand for the colatitude and longitude of the Northern pole of the geomagnetic dipole. Each file includes two models, describing the primary ionospheric field at ground and the secondary (induced) ionospheric field, as explained in Subsection 2.4. Each model is stored as a $N_d \times (2N_{sp})$ block of coefficients, where N_d (defined in Section 2.2) is the number of dipole coefficients for a given pair of diurnal and seasonal wavenumbers and $N_{sp} = (p_{\max} - p_{\min} + 1)(s_{\max} - s_{\min} + 1)$ is the number of such pairs. The first two columns contain the degree n and order m, respectively; positive (resp. negative) m values indicate that the line is that of coefficients to be multiplied by $\cos m\phi_d$ (resp. $\sin m\phi_d$) in the spherical harmonic expansion. In each line, coefficients are stored in columns 3 to $2N_{sp} + 2$, by iterating on s and p, in that order.

# Header							
# Header							
$N_{\max}$	$M_{\max}$	$p_{\min}$	$p_{\max}$	$s_{\min}$	$s_{\max}$	θ_{NGP}	ϕ_{NGP} h N
1	0	$q^{0(c)}_{1,s_{\min},p_{\min}}$	$q^{0(s)}_{1,s_{\min},p_{\min}}$	⋯	$q^{0(c)}_{1,s_{\max},p_{\max}}$	$q^{0(s)}_{1,s_{\max},p_{\max}}$	
1	1	$q^{1(c)}_{1,s_{\min},p_{\min}}$	$q^{1(s)}_{1,s_{\min},p_{\min}}$	⋯	$q^{1(c)}_{1,s_{\max},p_{\max}}$	$q^{1(s)}_{1,s_{\max},p_{\max}}$	
1	−1	$s^{1(c)}_{1,s_{\min},p_{\min}}$	$s^{1(s)}_{1,s_{\min},p_{\min}}$	⋯	$s^{1(c)}_{1,s_{\max},p_{\max}}$	$s^{1(s)}_{1,s_{\max},p_{\max}}$	
2	0	$q^{0(c)}_{2,s_{\min},p_{\min}}$	$q^{0(s)}_{2,s_{\min},p_{\min}}$	⋯	$q^{0(c)}_{2,s_{\max},p_{\max}}$	$q^{0(s)}_{2,s_{\max},p_{\max}}$	
2	1	$q^{1(c)}_{2,s_{\min},p_{\min}}$	$q^{1(s)}_{2,s_{\min},p_{\min}}$	⋯	$q^{1(c)}_{2,s_{\max},p_{\max}}$	$q^{1(s)}_{2,s_{\max},p_{\max}}$	
2	−1	$s^{1(c)}_{2,s_{\min},p_{\min}}$	$s^{1(s)}_{2,s_{\min},p_{\min}}$	⋯	$s^{1(c)}_{2,s_{\max},p_{\max}}$	$s^{1(s)}_{2,s_{\max},p_{\max}}$	
2	2	$q^{2(c)}_{2,s_{\min},p_{\min}}$	$q^{2(s)}_{2,s_{\min},p_{\min}}$	⋯	$q^{2(c)}_{2,s_{\max},p_{\max}}$	$q^{2(s)}_{2,s_{\max},p_{\max}}$	
2	−2	$s^{2(c)}_{2,s_{\min},p_{\min}}$	$s^{2(s)}_{2,s_{\min},p_{\min}}$	⋯	$s^{2(c)}_{2,s_{\max},p_{\max}}$	$s^{2(s)}_{2,s_{\max},p_{\max}}$	
⋯							
1	0	$g'^{0(c)}_{1,s_{\min},p_{\min}}$	$g'^{0(s)}_{1,s_{\min},p_{\min}}$	⋯	$g'^{0(c)}_{1,s_{\max},p_{\max}}$	$g'^{0(s)}_{1,s_{\max},p_{\max}}$	
1	1	$g'^{1(c)}_{1,s_{\min},p_{\min}}$	$g'^{1(s)}_{1,s_{\min},p_{\min}}$	⋯	$g'^{1(c)}_{1,s_{\max},p_{\max}}$	$g'^{1(s)}_{1,s_{\max},p_{\max}}$	
1	−1	$h'^{1(c)}_{1,s_{\min},p_{\min}}$	$h'^{1(s)}_{1,s_{\min},p_{\min}}$	⋯	$h'^{1(c)}_{1,s_{\max},p_{\max}}$	$h'^{1(s)}_{1,s_{\max},p_{\max}}$	
2	0	$g'^{0(c)}_{2,s_{\min},p_{\min}}$	$g'^{0(s)}_{2,s_{\min},p_{\min}}$	⋯	$g'^{0(c)}_{2,s_{\max},p_{\max}}$	$g'^{0(s)}_{2,s_{\max},p_{\max}}$	
2	1	$g'^{1(c)}_{2,s_{\min},p_{\min}}$	$g'^{1(s)}_{2,s_{\min},p_{\min}}$	⋯	$g'^{1(c)}_{2,s_{\max},p_{\max}}$	$g'^{1(s)}_{2,s_{\max},p_{\max}}$	
2	−1	$h'^{1(c)}_{2,s_{\min},p_{\min}}$	$h'^{1(s)}_{2,s_{\min},p_{\min}}$	⋯	$h'^{1(c)}_{2,s_{\max},p_{\max}}$	$h'^{1(s)}_{2,s_{\max},p_{\max}}$	
2	2	$g'^{2(c)}_{2,s_{\min},p_{\min}}$	$g'^{2(s)}_{2,s_{\min},p_{\min}}$	⋯	$g'^{2(c)}_{2,s_{\max},p_{\max}}$	$g'^{2(s)}_{2,s_{\max},p_{\max}}$	
2	−2	$h'^{2(c)}_{2,s_{\min},p_{\min}}$	$h'^{2(s)}_{2,s_{\min},p_{\min}}$	⋯	$h'^{2(c)}_{2,s_{\max},p_{\max}}$	$h'^{2(s)}_{2,s_{\max},p_{\max}}$	
⋯							

and $\left(d^{lm}_{kn}\right)^*$ are coefficients of the matrix relating spherical harmonics in dipole and quasi-dipole coordinates:

$$P^l_k(\theta_q)\exp(il\phi_q) = \sum_{n=1}^{N_{\max}} \sum_{m=-\min(n,M_{\max})}^{\min(n,M_{\max})} \left(d^{lm}_{kn}\right)^* P^m_n(\theta_d) \times \exp(im\phi_d) \quad (13)$$

Here $N_{\max}$ and $M_{\max}$ are chosen so that the convergence of the above summation is sufficient (see numerical values in the text below and Fig. 2). Equations (11) and (12) may be expressed in matrix form:

$$\boldsymbol{T_e} = \boldsymbol{D}^H \boldsymbol{U_e} \boldsymbol{S_e} \quad (14)$$

$$\boldsymbol{T_i} = \boldsymbol{D}^H \boldsymbol{U_i} \boldsymbol{S_i} \quad (15)$$

where $\boldsymbol{T_e}$ and $\boldsymbol{T_i}$ are the vectors of the $T^l_{ksp,e}$ and $T^l_{ksp,i}$, re-

Table 2. Residual statistics (in nT) for AR1 and AR2 tests.

Component	AR1 test	AR2 test
All data		
B_r	0.00 ± 0.15	0.01 ± 1.77
B_θ	0.00 ± 0.11	0.00 ± 2.88
B_ϕ	-0.01 ± 0.11	0.00 ± 2.37
$\lvert 90 - \theta_d \rvert \leq 55^\circ$		
B_r	0.00 ± 0.15	0.01 ± 1.78
B_θ	0.00 ± 0.10	-0.01 ± 2.75
B_ϕ	-0.01 ± 0.10	0.00 ± 2.04

spectively, $\boldsymbol{D}$ is the matrix of d_{kn}^{lm} coefficients, $\boldsymbol{U_e}$ is the diagonal matrix of $(a/(a+h))^{n-1}$ values, and $\boldsymbol{U_i}$ is the diagonal matrix of $((a+h)/a)^{n+2}$ values. It is worth noting that the spherical harmonics in QD coordinates are not orthogonal. By construction, the $T_{ksp,e}^{l}$ and $T_{ksp,i}^{l}$ functions have an exact QD geometry only on the sphere $r = a + h$. By analogy with Eqs. (4)–(5), the DIFI algorithm expresses the ionospheric magnetic potential in quasi-dipole coordinates as

$$V = Re\{\, \tilde{\epsilon}^H \boldsymbol{T_e} + \tilde{\iota}^H \boldsymbol{T_i}\} \quad \text{for } a < r < a + h \tag{16}$$

$$V = Re\{(\, \tilde{\epsilon}'^H + \tilde{\iota}^H)\boldsymbol{T_i}\} \quad \text{for } r > a + h \tag{17}$$

where $\tilde{\epsilon}$, $\tilde{\iota}$ and $\tilde{\epsilon}'$ are vectors of complex coefficients $(\tilde{\epsilon}_{ksp}^{l})^*$, $(\tilde{\iota}_{ksp}^{l})^*$ and $(\tilde{\epsilon}_{ksp}^{\prime l})^*$, respectively. This leads to the following constraints on the $\boldsymbol{\epsilon}$, $\boldsymbol{\iota}$ and $\boldsymbol{\epsilon}'$ vector of coefficients:

$$\boldsymbol{\epsilon} = \boldsymbol{U_e D}\, \tilde{\epsilon} \tag{18}$$

$$\boldsymbol{\iota} = \boldsymbol{U_i D}\, \tilde{\iota} \tag{19}$$

$$\boldsymbol{\epsilon}' = \boldsymbol{U_i D}\, \tilde{\epsilon}' \tag{20}$$

Combining (18)–(20) with (9)–(10) then leads to

$$V = Re\{\, \tilde{\epsilon}^H \boldsymbol{D}^H \boldsymbol{U_e}(\boldsymbol{S_e} + \boldsymbol{Q}^H \boldsymbol{S_i})\} \quad \text{for } a < r < a + h \tag{21}$$

$$V = Re\{\, \tilde{\epsilon}^H \boldsymbol{D}^H \boldsymbol{U_e}(\boldsymbol{C} + \boldsymbol{Q}^H)\boldsymbol{S_i}\} \quad \text{for } r > a + h \tag{22}$$

It is also assumed that the ionospheric magnetic field responds linearly to solar activity, parameterized by the solar radio flux index $F_{10.7}$ (expressed in solar flux units, or SFU, where 1 SFU $= 10^{-22}$ W m^{-2} Hz^{-1}). Then $\tilde{\epsilon}$ is replaced by $\tilde{\epsilon}(1 + N \times F_{10.7})$, where the so-called Wolf ratio $N = 14.85 \times 10^{-3}$ SFU^{-1} was determined by Olsen *et al.* (1993). It is worth noting that the Wolf ratio actually varies with season (see, e.g., Penquerc'h and Chulliat, 2009). This effect will be investigated during the *Swarm* mission and could lead us to develop a more sophisticated parameterization of the response to solar activity in later DIFI models.

The quasi-dipole vector of coefficients $\tilde{\epsilon}$ in (21)–(22) is truncated for $1 \leq k \leq K_{\max}$, $-\min(k, L_{\max}) \leq l \leq \min(k, L_{\max})$, $s_{\min} \leq s \leq s_{\max}$ and $p_{\min} \leq p \leq p_{\max}$. The dipole vector of coefficients $\boldsymbol{\epsilon}$ in (9)–(10) (as well as (18)) is truncated for $1 \leq n \leq N_{\max}$, $-\min(n, M_{\max}) \leq m \leq \min(n, M_{\max})$, $s_{\min} \leq s \leq s_{\max}$ and $p_{\min} \leq p \leq p_{\max}$. This leads to a total of $N_q = L_{\max}(L_{\max} + 2) + (K_{\max} - L_{\max})(2L_{\max} + 1)$ quasi-dipole coefficients and $N_d = M_{\max}(M_{\max} + 2) + (N_{\max} - M_{\max})(2M_{\max} + 1)$ dipole coefficients for each pair of wavenumbers (p, s). In the tests reported in Section 3, the ionospheric field was modelled in quasi-dipole coordinates up to degree $K_{\max} = 45$ and order $L_{\max} = 5$ (hence $N_q = 475$ coefficients), with diurnal variations from $p_{\min} = 0$ to $p_{\max} = 4$ (i.e., down to

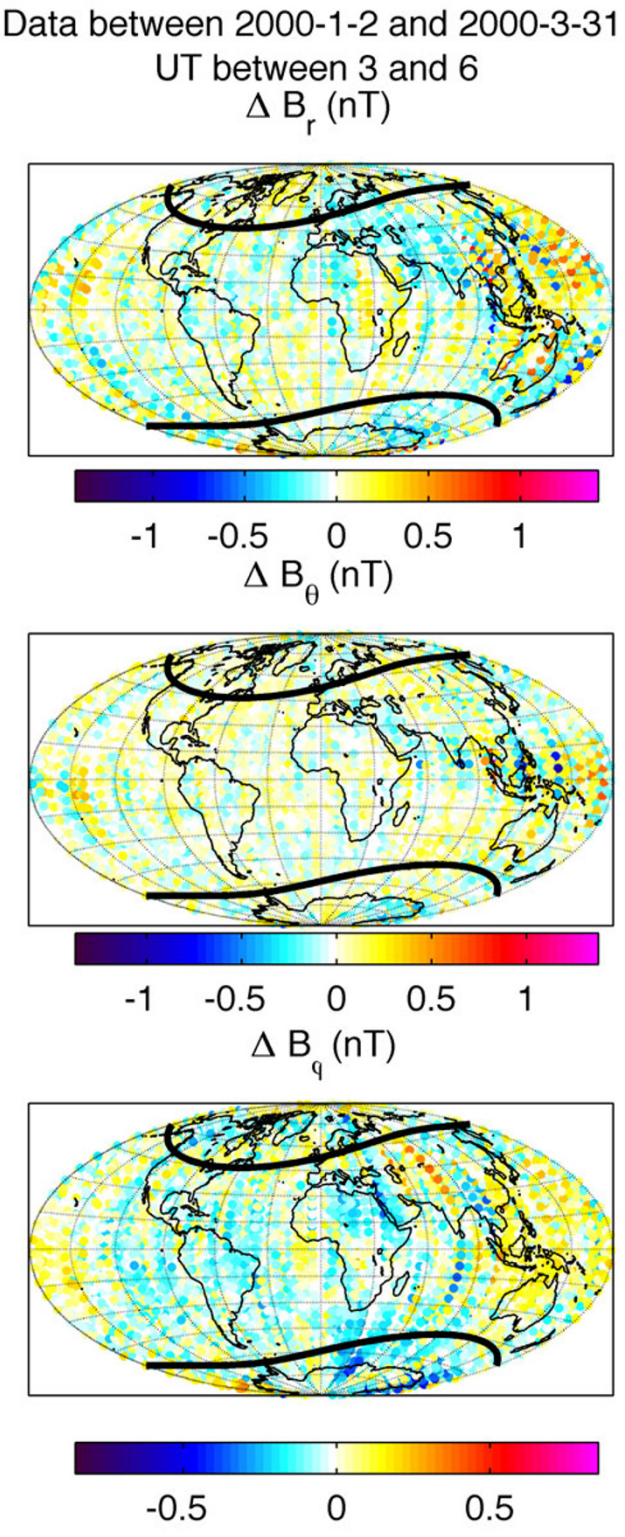

Fig. 3. Example of data residual maps, AR1 test. The parallels of dipole latitudes ±55° are represented as thick black lines.

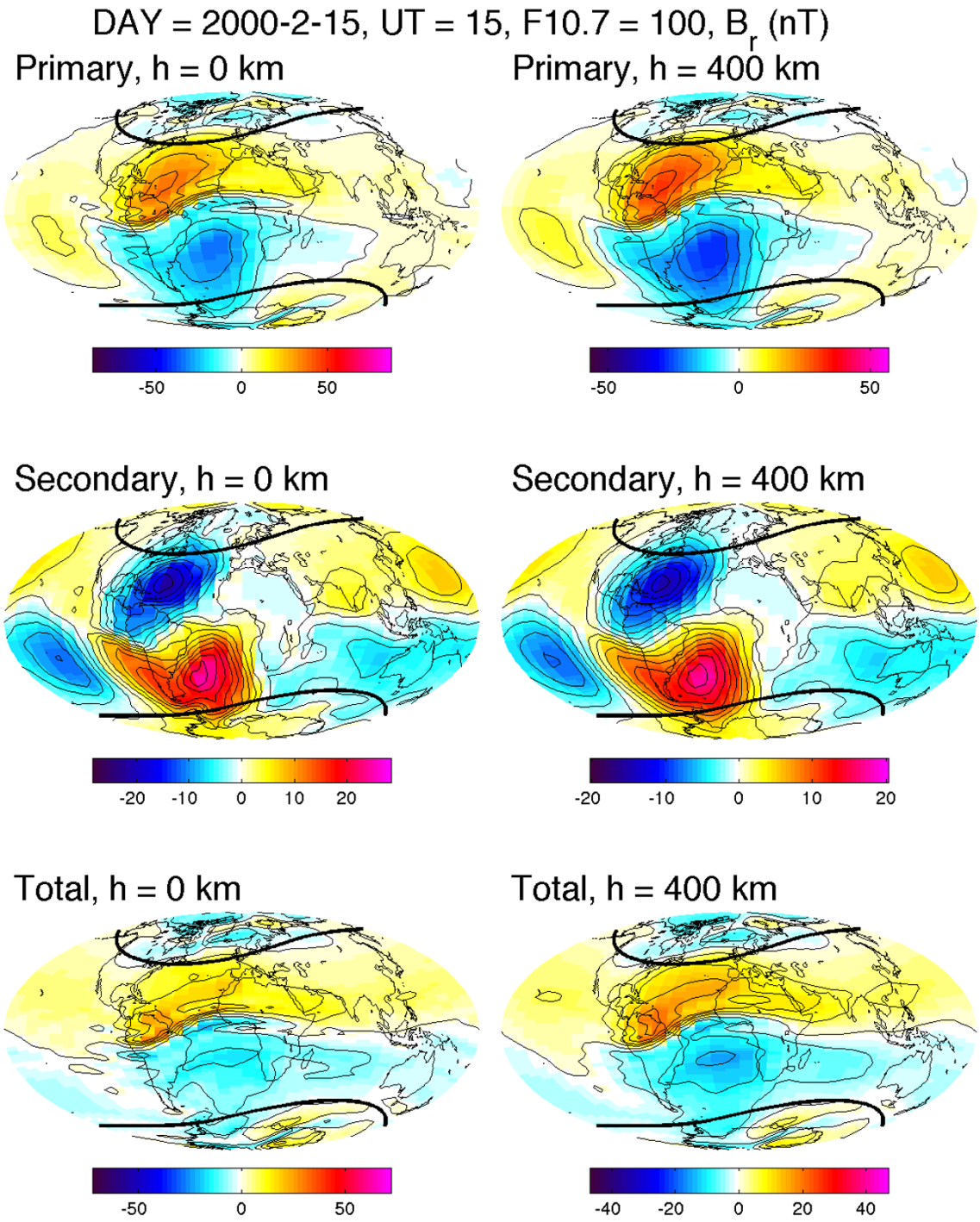

Fig. 4. Example of ionospheric field maps, B_r component, AR1 test. The parallels of dipole latitudes $\pm 55^\circ$ are represented as thick black lines.

a period of 6 hours) and seasonal variations from $s_{\min} = -2$ to $s_{\max} = 2$ (i.e., constant, annual and semi-annual variation). These parameters are the ones set in the original SCARF specifications (*Swarm* Level 2 Processing System Consortium, 2013). Note that p is arbitrarily taken positive, so that modes propagate westward for $l > 0$ (or $m > 0$) and eastward for $l < 0$ (or $m < 0$). Unlike Sabaka *et al.* (2000, 2002), we do not select only modes closest to the local time modes $l = p$. A numerical investigation of Eq. (13) shows that $N_{\max} = 60$ and $M_{\max} = 12$ (hence $N_d = 1368$ coefficients) are sufficient to achieve convergence of the $\boldsymbol{D}$ matrix. The modulus of the obtained matrix is shown in Fig. 2.

2.3 Inversion

The "building and solving of normal equations" block of the DIFI algorithm (Fig. 1) uses a standard iterative least squares technique to find a model solution that minimizes the following objective function:

$$\Phi(\tilde{\epsilon}) = [\gamma - \boldsymbol{f}(\tilde{\epsilon})]^H \boldsymbol{C}_e^{-1} [\gamma - \boldsymbol{f}(\tilde{\epsilon})] + \lambda\, \tilde{\epsilon}^H \boldsymbol{C}_m^{-1} \tilde{\epsilon} \qquad (23)$$

where γ is the data vector, $\boldsymbol{f}(\tilde{\epsilon})$ the data estimate vector calculated from the model, $\boldsymbol{C}_e$ the data covariance matrix, λ

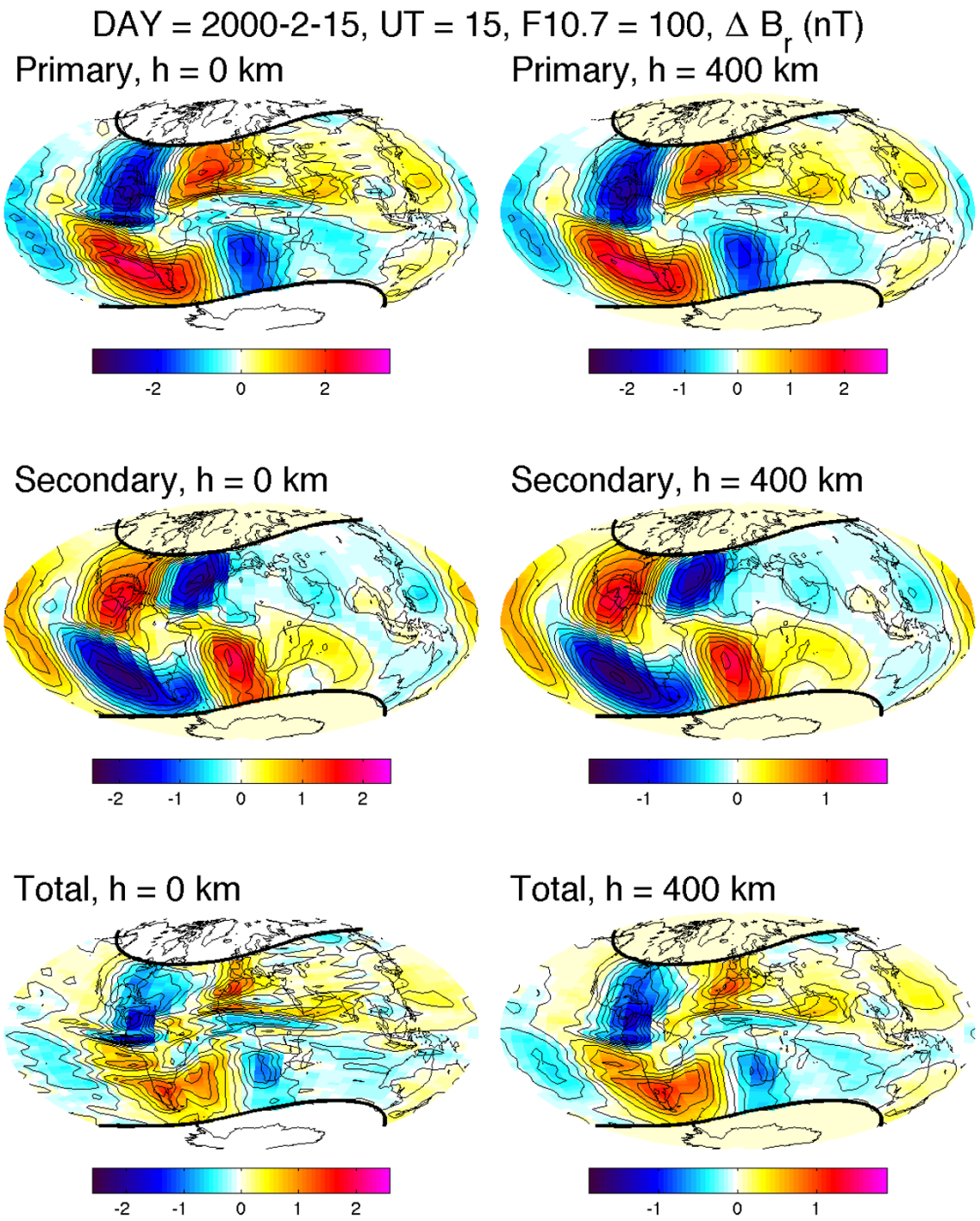

Fig. 5. Example of maps showing field differences, B_r component, AR1 test. The parallels of dipole latitudes $\pm 55^\circ$ are represented as thick black lines.

a damping parameter and $\boldsymbol{C}_m$ a damping matrix. For the purpose of the tests based upon synthetic data, we used an identity matrix for the data covariance matrix, and set the damping parameter to zero. These choices will be revised during the exploitation phase, when real data will be considered. We anticipate that the actual data covariance matrix will be diagonal, assuming that the data noise is caused by stationary and uncorrelated processes. For each data type (satellite and observatory) and each component, variances will be iteratively determined, starting from an existing Sq field model. Regarding the damping matrix, a simple, diagonal matrix will first be used, to minimize those coefficients that will be found less constrained by the data. If needed, more sophisticated damping strategies will be used, such as minimizing night-time ionospheric currents (Sabaka *et al.*, 2002).

2.4 Output

In order to facilitate the distribution and use of the ionospheric field models produced by the *Swarm* SCARF, it was decided to distribute them as sets of real Gauss coefficients in dipole coordinates. The same format is to be used for both the comprehensive and dedicated chains. Specifically,

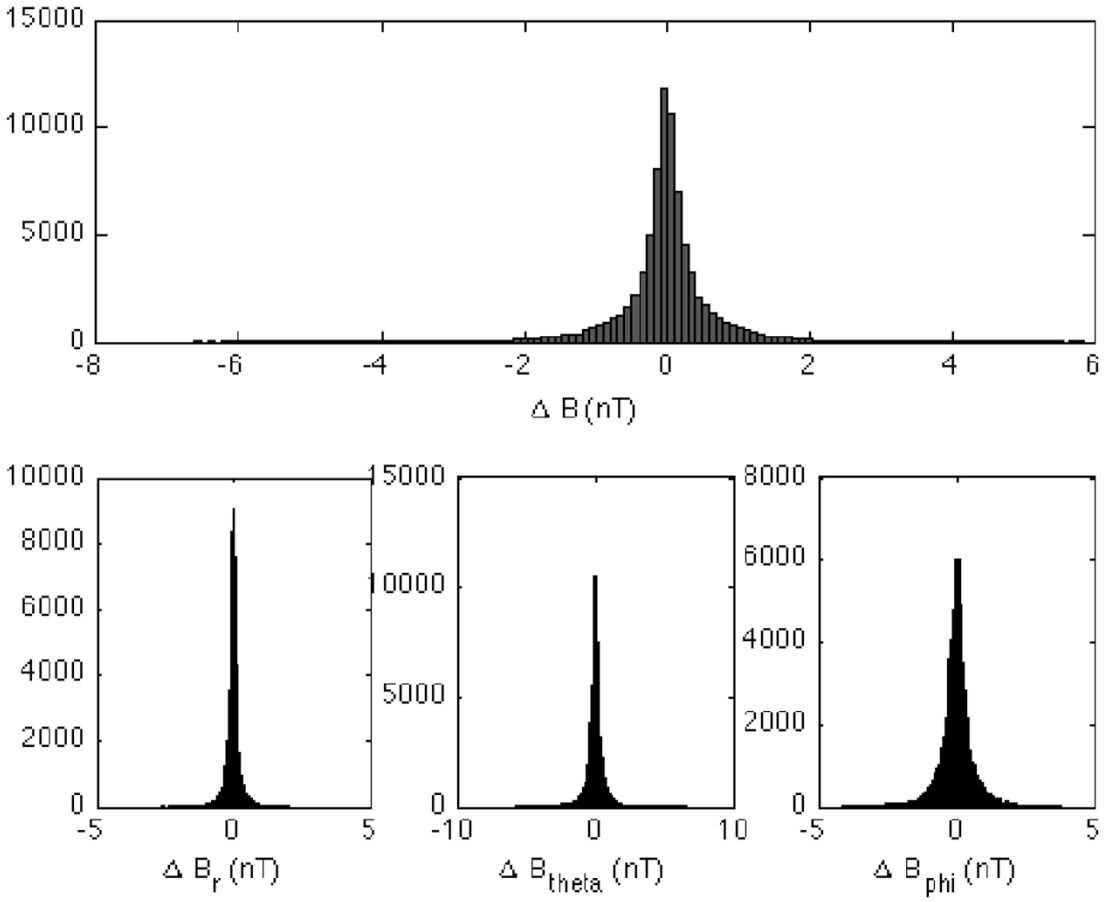

Fig. 6. Distribution of non-polar field differences, AR1 test. B is the modulus of the field.

the scalar potential V_1 of the primary ionospheric field is expressed as:

$$\begin{aligned} V_1(r,\theta_d,\phi_d,t,t_m) &= (1+N\times F_{10.7}) \\ &\times \sum_{s=s_{\min}}^{s_{\max}}\sum_{p=p_{\min}}^{p_{\max}}\sum_{n=1}^{N_{\max}}\sum_{m=0}^{M_{\max}} a\left(\frac{r}{a}\right)^n P_n^m(\theta_d) \\ &\times \left\{\left[q_{nsp}^{m(c)}\cos m\phi_d + s_{nsp}^{m(c)}\sin m\phi_d\right]\right. \\ &\times \cos(\omega_s s t+\omega_p p t_m) \\ &+ \left[q_{nsp}^{m(s)}\cos m\phi_d + s_{nsp}^{m(s)}\sin m\phi_d\right] \\ &\times \left.\sin(\omega_s s t+\omega_p p t_m)\right\} \\ &\quad \text{for } a<r<a+h \end{aligned} \tag{24}$$

$$\begin{aligned} V_1(r,\theta_d,\phi_d,t,t_m) &= (1+N\times F_{10.7}) \\ &\times \sum_{s=s_{\min}}^{s_{\max}}\sum_{p=p_{\min}}^{p_{\max}}\sum_{n=1}^{N_{\max}}\sum_{m=0}^{M_{\max}} a\left(\frac{a}{r}\right)^{n+1} P_n^m(\theta_d) \\ &\times \left\{\left[g_{nsp}^{m(c)}\cos m\phi_d + h_{nsp}^{m(c)}\sin m\phi_d\right]\right. \\ &\times \cos(\omega_s s t+\omega_p p t_m) \\ &+ \left[g_{nsp}^{m(s)}\cos m\phi_d + h_{nsp}^{m(s)}\sin m\phi_d\right] \\ &\times \left.\sin(\omega_s s t+\omega_p p t_m)\right\} \\ &\quad \text{for } r>a+h \end{aligned} \tag{25}$$

where $q_{nsp}^{m(c,s)}$, $s_{nsp}^{m(c,s)}$, $g_{nsp}^{m(c,s)}$ and $h_{nsp}^{m(c,s)}$ are real coefficients. Note that the $q_{nsp}^{m(c,s)}$, $s_{nsp}^{m(c,s)}$ (resp. the $g_{nsp}^{m(c,s)}$, $h_{nsp}^{m(c,s)}$) are obtained by taking the real part of the product $\boldsymbol{\epsilon}^{\prime H}\boldsymbol{S_e}$ in Eq. (4) (resp. the product $\boldsymbol{\epsilon}^{\prime H}\boldsymbol{S_i}$ in Eq. (5)).

The scalar potential V_2 of the secondary (induced) ionospheric field is expressed as in Eq. (25), but with real coefficients $g_{nsp}^{\prime m(c,s)}$, $h_{nsp}^{\prime m(c,s)}$; these are obtained by taking the real part of the product $\boldsymbol{\iota}^H\boldsymbol{S_i}$ in Eqs. (4)–(5).

Equations (7)–(8) relate the coefficients below and above the ionosphere in Eqs. (24)–(25). Therefore, only coefficients $q_{nsp}^{m(c,s)}$, $s_{nsp}^{m(c,s)}$, $g_{nsp}^{\prime m(c,s)}$ and $h_{nsp}^{\prime m(c,s)}$ are provided in the MIO_SHA product files. The exact format of these files is given in Table 1 (and can also be found in the product specification document, *Swarm* Level 2 Processing System Consortium, 2013).

3. Test Results

During the preparation phase, the DIFI algorithm was tested using synthetic data. The way the synthetic orbits and magnetic data were generated is described in Olsen *et al.* (2013). We used only one year of synthetic data, from January 1, 2000 to December 31, 2000, and relied on real K_p, D_{st}, IMF and $F_{10.7}$ values for the selected period.

The synthetic data were selected using the following criteria: $K_p \le 2o$, -20 nT $\le D_{st} \le 20$ nT, -8 nT $\le$

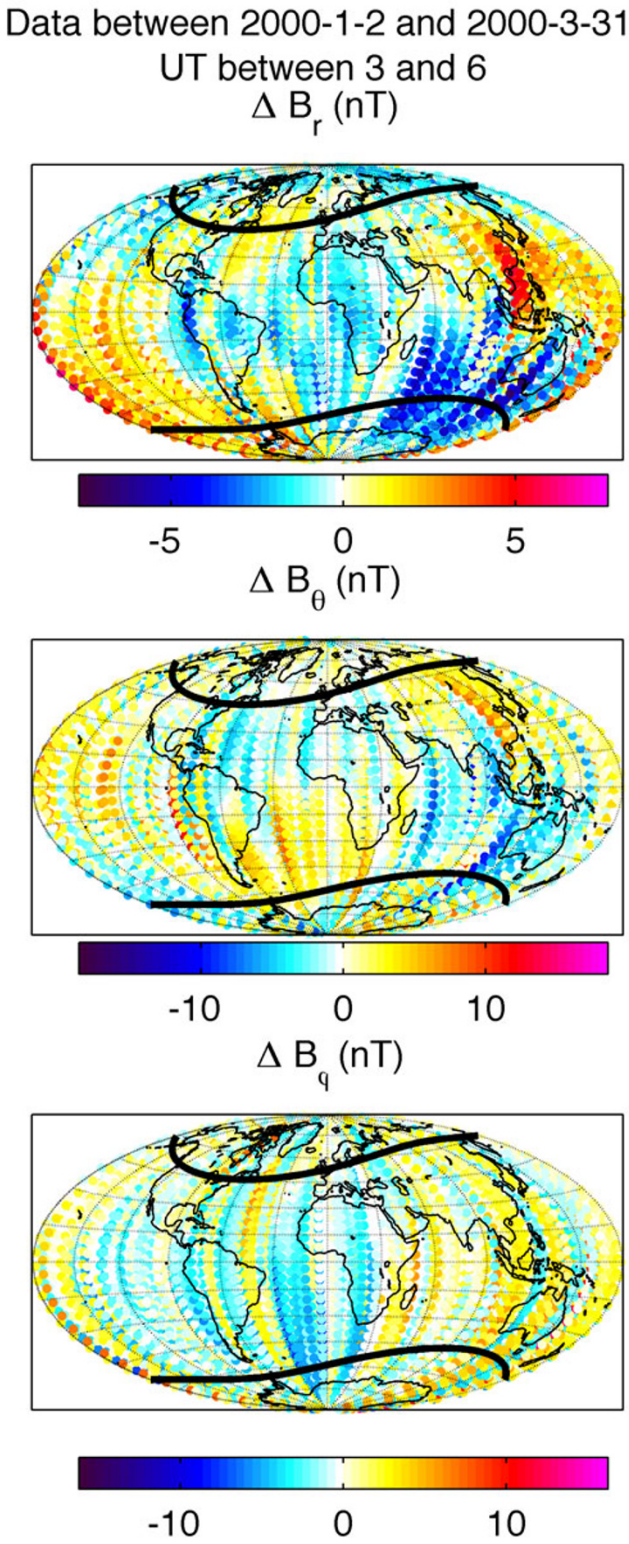

Fig. 7. Example of data residual maps, AR2 test. The parallels of dipole latitudes ±55° are represented as thick black lines.

IMF $B_y \leq 8$ nT and -2 nT $\leq$ IMF $B_z \leq 6$ nT. Starting from synthetic Level 1b 1 Hz data, the selection process lead to 583705 data triples for each satellite A and C. The data were further decimated so that the time difference between two successive data never fell below 15 s, which corresponds to a minimum distance of about 105 km (since *Swarm* satellites orbit at about 7 km/s).

Removal of non-ionospheric contributions were implemented in different ways, depending on the tests carried out. During the so-called "AR1 test", data were corrected using the same reference field models as the ones used for generating the synthetic data (see Olsen *et al.*, 2013, for details about these models). As the random noise added to the synthetic data had a very small standard deviation (between 0.1 and 0.7 nT, depending on the component) compared to the typical amplitude of ionospheric fields, the data after correction were very close to the synthetic ionospheric field data themselves. Thus, the AR1 test essentially amounted to a closed-loop simulation of both the pre-processing and inversion blocks. During the second, so-called "AR2 test", data were corrected using core, lithospheric and magnetospheric field models derived as part of the test by SCARF partners, thus imperfectly reproducing the contribution of each source to the synthetic data, as would be the case with real data.

For both tests, we used the same $\boldsymbol{Q}$ matrix as the one used for generating the synthetic dataset (see Olsen *et al.*, 2013, for details). This matrix was derived from a 3D electrical conductivity model of the mantle, including oceans, designed by Kuvshinov *et al.* (2006). We used the $\boldsymbol{D}$ matrix already mentioned in Section 2.2 and presented in Fig. 2.

3.1 AR1 test

Data residuals statistics for the AR1 test are presented in Table 2. The means of the data residuals are close to zero; the standard deviations are of the same order of magnitude or smaller than the noise added to the synthetic data, for all three components. This suggests that the closed-loop test was successful. Still, it is important to also check the maps of data residuals for various universal times (UT) and seasons, as these could reveal very localized (in space or time) discrepancies from the data. We divided the year in four seasons and the day in 8 UT intervals, plotting a total of 32 maps for each component. A careful examination of the maps did not reveal any anomaly. An example of data residual maps for the three components is shown in Fig. 3.

Data residuals, however, do not provide all the information needed to check the validity of the DIFI-derived model. The obtained model has to be valid at ground level as well as at satellite altitude, and its separation into primary and induced fields has to be correct. This can be checked by plotting maps of differences between the field calculated from the reference model (used to produce the synthetic data) and the DIFI-derived model. We again plotted 32 maps at different seasons and UT for each component, each type of field (primary, induced and total) and at 0 and 400 km altitude. Examples of such maps showing the radial component of the ionospheric field and associated field differences are shown in Figs. 4 and 5. Note that the color scales were calculated from the absolute minima and maxima found in the 32 maps of the same kind. As expected, differences are smallest for the total field at satellite altitude, i.e., where the model is most constrained by the data. The total field differences at satellite altitude are slightly larger than the residuals for the same season (Fig. 3), which suggests some possible effect of incomplete data coverage. For seasons having better data coverage, e.g., Spring, the total field differences

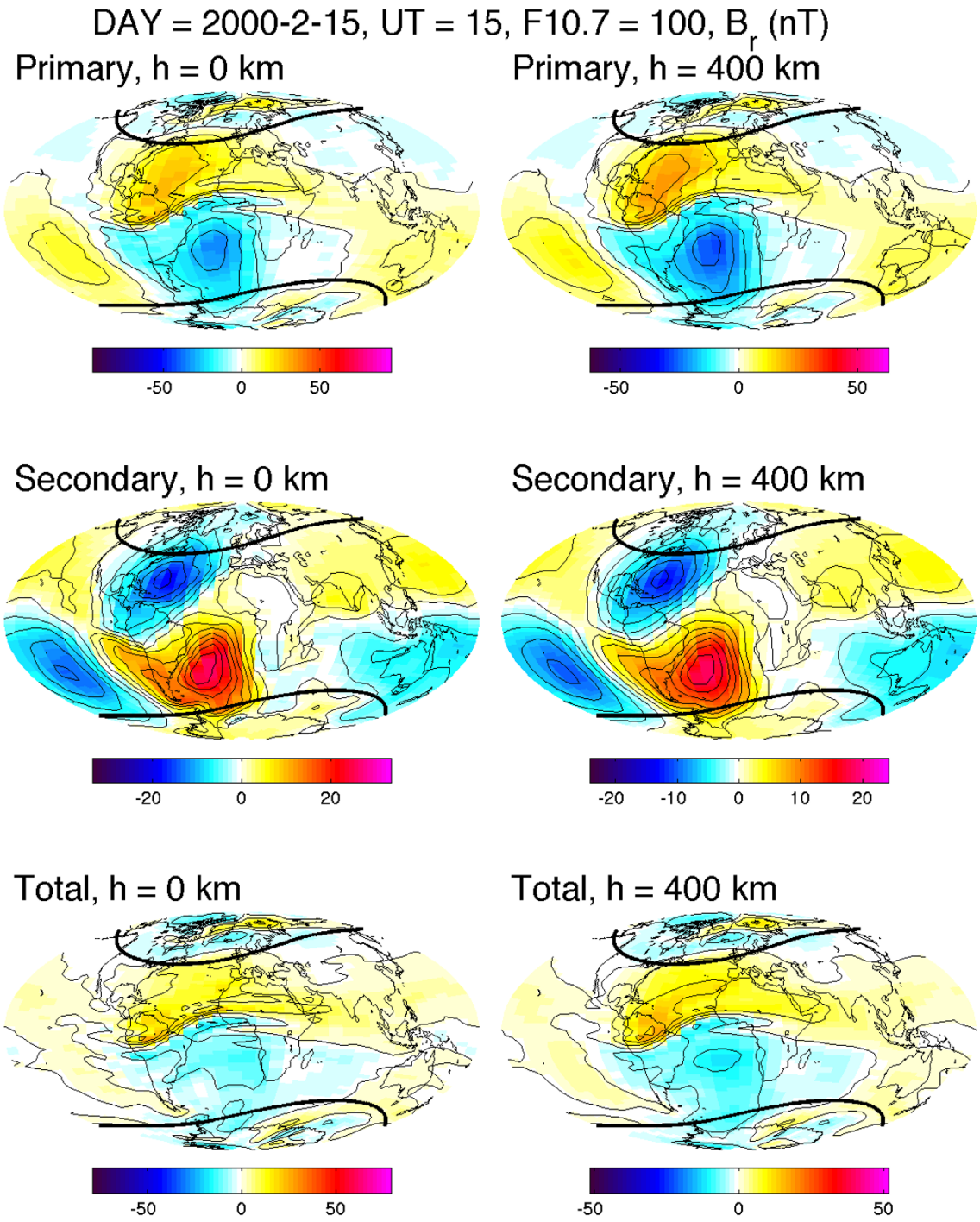

Fig. 8. Example of ionospheric field maps, B_r component, AR2 test. The parallels of dipole latitudes $\pm 55^\circ$ are represented as thick black lines.

are indeed smaller (less than 1 nT). Interestingly, the differences in the primary and secondary fields are of opposite signs and partially cancel out each other; this could be due to the fact that no damping was applied in this run. Also, there is a prominent four-spot structure for the radial component, indicating some slight deformation of the Northern and Southern foci of the Sq field.

A more synthetic view of the model error at the Earth's surface is provided by Fig. 6, which shows the distribution of differences at non-polar latitudes ($|90 - \theta_d| \leq 55^\circ$). To produce this figure, differences were calculated on a regular grid, for 8 three-hour universal time bins and 40 seasonal bins. (Although one seasonal bin per day should be used to account for differences caused by day-to-day magnetospheric field fluctuations, this number is not critical when using synthetic data and will be adjusted during the operational phase.) For each component, the standard deviation of these differences divided by the maximum field value (from all bins) is taken as a measure of the model performance. Numerical results are provided in Table 3. It can be checked that the performances are below 2%, which is well below the threshold requirement of 10% (see table 5 in

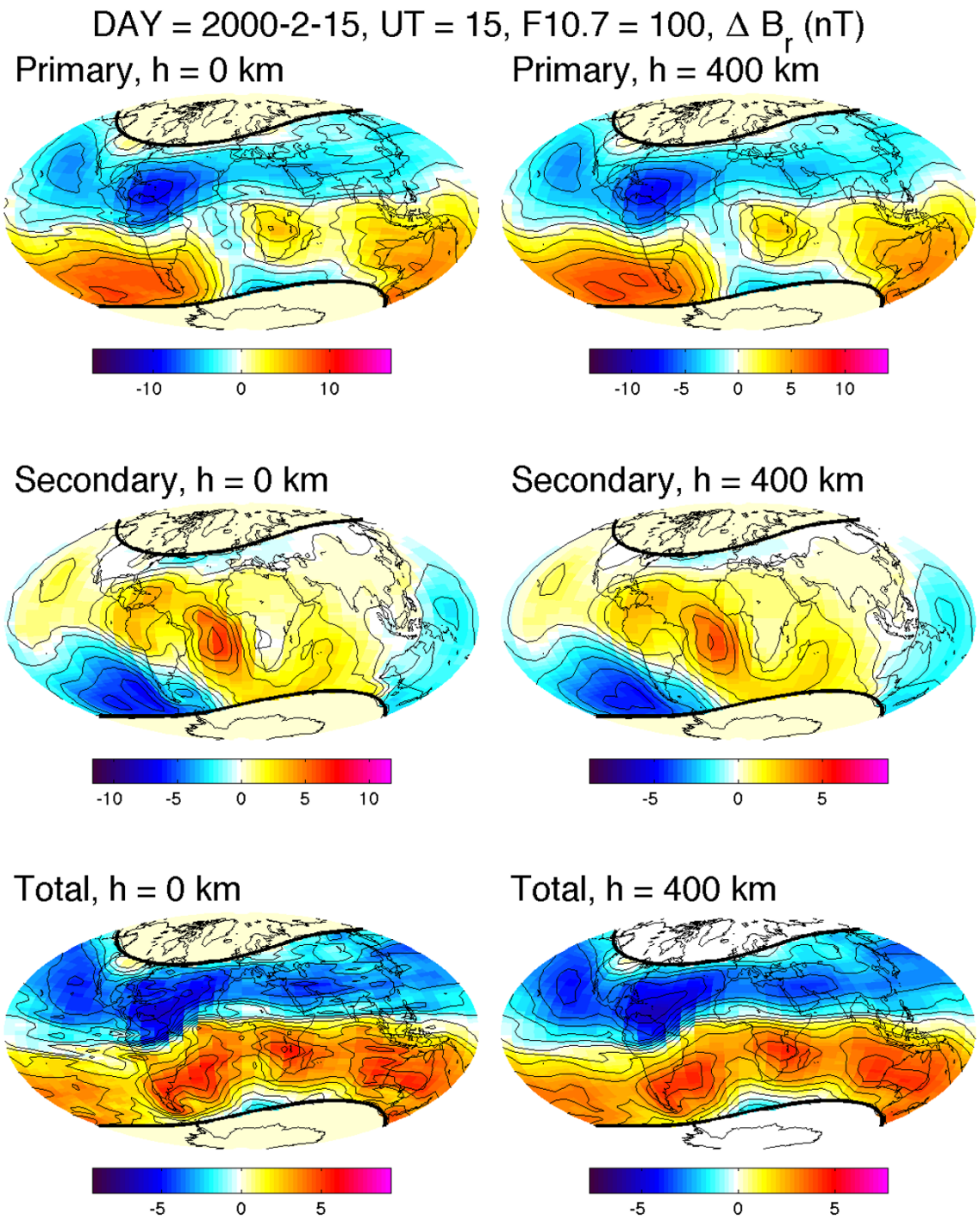

Fig. 9. Example of maps showing field differences, AR2 test. The parallels of dipole latitudes ±55° are represented as thick black lines.

Olsen *et al.*, 2013). These numbers can be seen as the maximum performance achievable by the current version of the DIFI chain.

3.2 AR2 test

For the AR2 test, data corrections relied on the dedicated core (Rother *et al.*, 2013) and lithospheric (Thébault *et al.*, 2013) field models, and the magnetospheric part of the comprehensive (Sabaka *et al.*, 2013) field model, all of them derived from the AR2 dataset. Data residuals statistics (see Table 2) show that using imperfect field models for data correction leads to significant residuals after the inversion. This is confirmed by the analysis of residuals maps; see for example Fig. 7, which was selected for the same season and UT as Fig. 3 in order to facilitate comparison.

Like for the AR1 test, we plotted maps of the field calculated from the DIFI-derived model and of the differences between that field and the reference field. Examples of such maps are shown in Figs. 8 and 9. Note that the color scales were again calculated from the extrema in the 32 maps of the same kind (at different seasons and UT). The imperfect data correction leads to much larger differences between the reference model and the DIFI-derived model than those ob-

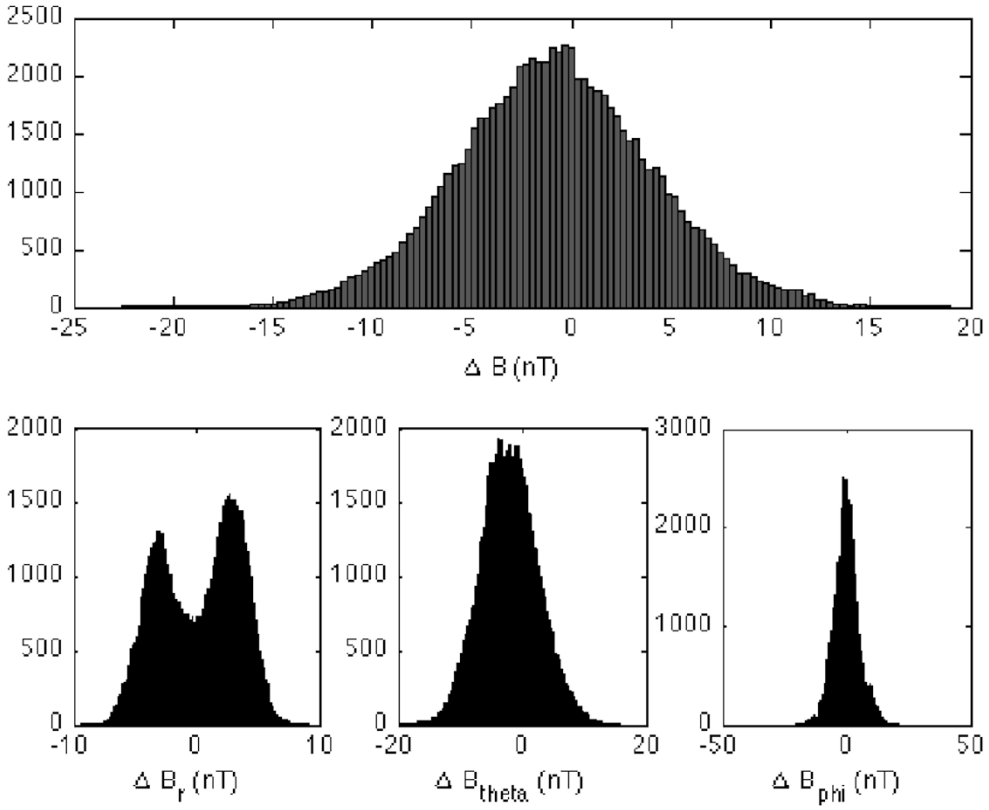

Fig. 10. Distribution of non-polar field differences, AR2 test. B is the modulus of the field.

Table 3. Model performances (as defined in the main text) for AR1 and AR2 tests.

Component	AR1 test	AR2 test
B_r	0.75%	8.93%
B_θ	1.56%	10.4%
B_ϕ	1.90%	14.6%
B	0.65%	4.67%

tained in the AR1 test. The differences for the total field are antisymmetrical with respect to the magnetic dip equator and are rather uniformly distributed in local time. This pattern is also observed at other local times and seasons, but the position of extrema is not always linked to the Sq foci, unlike in the example shown in Fig. 9. This probably reflects the leakage of the core and magnetospheric fields in the ionospheric field model, since these two fields are not, or only weakly, local-time-dependent. As in the AR1 case, the differences for the primary and secondary fields are larger than for the total field, which is probably due to the absence of damping. The spatial pattern of the differences for these fields greatly varies with season and local time and is therefore difficult to interpret.

The imperfect data correction also affects the overall performance of the model at the Earth's surface (see Table 3). The performance is below or slightly above the threshold requirement of 10% (Olsen *et al.*, 2013). Plotting the distribution of non-polar differences at the Earth's surface (Figure 10) reveals two bumps in the B_r distribution, around 4 nT, as well as some bias of a few nT in B_θ and the scalar field. The bumps are also present when plotting the output of the pre-processing block; i.e., they are not caused by the inversion. We found that they originate in the imperfect correction for the core field.

4. Concluding Remarks

In the present paper, we described the algorithm of the DIFI chain to be used during the upcoming *Swarm* mission to calculate global, spherical harmonic models of the quiet-time ionospheric field at mid-to-low latitudes. This algorithm relies on quasi-dipole coordinates to minimize the number of parameters, while describing the smallest spatial features of the average field such as the equatorial electrojet. It can take advantage of a 3D conductivity model of the mantle and oceans when separating the primary and induced fields.

Closed-loop tests using synthetic data showed that the DIFI algorithm is able to reproduce the original primary and induced ionospheric fields to a very high accuracy, at ground and satellite altitudes. Tests relying on other SCARF models produced from the same dataset for data correction of the core, lithospheric and magnetospheric fields revealed that the pre-processing block of the algorithm is very sensitive to the quality of the correcting models. This problem is specific to the DIFI chain, as this chain is the last in the sequence of dedicated inversion chains to be processed. As a result, all errors made by previous chains

in the sequence cascade down to the DIFI input. However, the inversion block proved remarkably stable with respect to these input errors; it is possible to calculate a meaningful ionospheric field, with performances within the threshold requirement, even when starting from imperfectly corrected data. During the exploitation phase, no reference field will be available to validate the DIFI chain output. The validation will be made by comparing the total field at ground with measurements from geomagnetic observatories.

Acknowledgments. The research reported here was financially supported by the Centre National d'Etudes Spatiales (CNES) through the "Travaux préparatoires et exploitation de la mission *Swarm*" project, and by the European Space Agency (ESA) through ESTEC contract 4000102140/10/NL/JA "Development of the *Swarm* Level 2 Algorithms and Associated Level 2 Processing Facility". The authors thank the reviewers for their very helpful comments. This is IPGP contribution number 3423.

References

Alken, P., S. Maus, P. Vigneron, O. Sirol, and G. Hulot, Swarm SCARF equatorial electric field inversion chain, *Earth Planets Space*, **65**, this issue, 1309–1317, 2013.

Emmert, J. T., A. D. Richmond, and D. P. Drob, A computationally compact representation of Magnetic-Apex and Quasi-Dipole coordinates with smooth base vectors, *J. Geophys. Res.*, **115**(A8), 1–13, doi:10.1029/2010JA015326, 2010.

Friis-Christensen, E., H. Lühr, and G. Hulot, *Swarm*: A constellation to study the Earth's magnetic field, *Earth Planets Space*, **58**, 351—358, 2006.

Kuvshinov, A., T. Sabaka, and N. Olsen, 3-D electromagnetic induction studies using the *Swarm* constellation: Mapping conductivity anomalies in the Earth's mantle, *Earth Planets Space*, **58**, 417—427, 2006.

Hamilton, B., Rapid modelling of the large-scale magnetospheric field from Swarm satellite data, *Earth Planets Space*, **65**, this issue, 1295–1308, 2013.

Macmillan, S. and N. Olsen, Observatory data and the Swarm mission, *Earth Planets Space*, **65**, this issue, 1355–1362, 2013.

Olsen, N., The solar cycle variability of lunar and solar daily geomagnetic variations, *Ann. Geophys.*, **11**, 254–262, 1993.

Olsen, N., E. Friis-Christensen, R. Floberghagen, P. Alken, C. D Beggan, A. Chulliat, E. Doornbos, J. T. da Encarnação, B. Hamilton, G. Hulot, J. van den IJssel, A. Kuvshinov, V. Lesur, H. Lühr, S. Macmillan, S. Maus, M. Noja, P. E. H. Olsen, J. Park, G. Plank, C. Püthe, J. Rauberg, P. Ritter, M. Rother, T. J. Sabaka, R. Schachtschneider, O. Sirol, C. Stolle, E. Thébault, A. W. P. Thomson, L. Tøffner-Clausen, J. Velímský, P. Vigneron, and P. N. Visser, The *Swarm* Satellite Constellation Application and Research Facility (SCARF) and *Swarm* data products, *Earth Planets Space*, **65**, this issue, 1189–1200, 2013.

Penquerc'h, V. and A. Chulliat, Variability of the Sq magnetic field with the solar radiation flux F10.7, in *Proceedings of ESA's Second Swarm International Science Meeting*, 2009.

Richmond, A. D., Ionospheric electrodynamics using magnetic apex coordinates, *J. Geomag. Geoelectr.*, **47**, 191–212, doi:10.5636/jgg.47.191, 1995.

Richmond, A. D. and J. P. Thayer, Ionospheric electrodynamics: A tutorial, in *Magnetospheric Current Systems*, Geophysical Monograph 118, American Geophysical Union, 131–146, 2000.

Rother, M., V. Lesur, and R. Schachtschneider, An algorithm for deriving core magnetic field models from the Swarm data set, *Earth Planets Space*, **65**, this issue, 1223–1231, 2013.

Sabaka, T. J., N. Olsen, and R. A. Langel, A comprehensive model of the near-Earth magnetic field: Phase 3, NASA/TM-2000-209894, 1–75, 2000.

Sabaka, T. J., N. Olsen, and R. A. Langel, A comprehensive model of the quiet-time, near-Earth magnetic field: Phase 3, *Geophys. J. Int.*, **151**, 32–68, doi:10.1046/j.1365-246X.2002.01774.x, 2002.

Sabaka, T. J., N. Olsen, and M. E. Purucker, Extending comprehensive models of the Earth's magnetic field with Ørsted and CHAMP data, *Geophys. J. Int.*, **159**, 521–547, doi:10.1111/j.1365-246X.2004.02421.x, 2004.

Sabaka, T. J., L. Tøffner-Clausen, and N. Olsen, Use of the Comprehensive Inversion method for *Swarm* satellite data analysis, *Earth Planets Space*, **65**, this issue, 1201–1222, 2013.

Schmucker, U., A spherical harmonic analysis of solar daily variations in the years 1964–1965: Response estimates and source fields for global induction—I. Methods, *Geophys. J. Int.*, **136**, 439–454, doi:10.1046/j.1365-246X.1999.00742.x, 1999a.

Schmucker, U., A spherical harmonic analysis of solar daily variations in the years 1964–1965: Response estimates and source fields for global induction—II. Results, *Geophys. J. Int.*, **136**, 455–476, doi:10.1046/j.1365-246X.1999.00743.x, 1999b.

Swarm Level 2 Processing System Consortium, Product specification for L2 Products and Auxiliary Products, Doc. no: SW-DS-DTU-GS-0001, 2013.

Takeda, M., Features of global geomagnetic Sq field from 1980 to 1990, *J. Geophys. Res.*, **107**(A9), 1–8, doi:10.1029/2001JA009210, 2002.

Thébault, E., P. Vigneron, S. Maus, A. Chulliat, O. Sirol, and G. Hulot, Swarm SCARF Dedicated Lithospheric Field Inversion chain, *Earth Planets Space*, **65**, this issue, 1257–1270, 2013.

A. Chulliat (e-mail: chulliat@ipgp.fr), P. Vigneron, E. Thébault, O. Sirol, and G. Hulot